

Strain-engineered artificial atom as a broad-spectrum solar energy funnel

Ji Feng^{1†}, Xiaofeng Qian^{2†}, Cheng-Wei Huang² and Ju Li^{2,3*}

An optoelectronic material with a spatially varying bandgap that is tunable is highly desirable for use in photovoltaics, photocatalysis and photodetection. Elastic strain has the potential to be used to achieve rapid and reversible tuning of the bandgap. However, as a result of plasticity or fracture, conventional materials cannot sustain a high enough elastic strain to create sufficient changes in their physical properties. Recently, an emergent class of materials—named ‘ultrastrength materials’—have been shown to avoid inelastic relaxation up to a significant fraction of their ideal strength. Here, we illustrate theoretically and computationally that elastic strain is a viable agent for creating a continuously varying bandgap profile in an initially homogeneous, atomically thin membrane. We propose that a photovoltaic device made from a strain-engineered MoS₂ monolayer will capture a broad range of the solar spectrum and concentrate excitons or charge carriers.

The ability to continuously control the bandgap in optoelectronic materials, in a low-cost manner, is highly desirable for a wide range of energy and sensing applications, including photovoltaics^{1–3}, photocatalysis⁴ and photodetection⁵. For example, the efficiency of photovoltaic devices comprising a single p–n junction is subject to the thermodynamic constraint of the Shockley–Queisser limit¹, as only a limited portion of solar energy can be absorbed. Although tandem solar cells consisting of multi-junctions with cascaded bandgaps can achieve higher absorption efficiencies, the increased complexity of their fabrication and the high cost of materials are major drawbacks. It would therefore be a great advantage if one could fine-tune the bandgap within a single semiconducting material. Like chemical composition, elastic strain is a continuous variable that is capable of altering many physical and chemical properties. Although elastic strain engineering is a straightforward concept, its potential in photonics remains largely under-exploited. The key hurdle is the fact that conventional bulk-scale materials cannot sustain a high enough elastic strain to induce sufficient changes to the physical properties before they deform plastically or break.

Recently, materials belonging to an emergent class termed ‘ultrastrength materials’^{6–8} have been found to avoid inelastic relaxation up to a significant fraction of their ideal strengths; that is, materials of different size and dimensionality can exhibit dramatically distinct physical and chemical properties as well as mechanical strengths. Atomically thin membranes are a notable family of materials that exhibit the property of ultrastrength^{8,9}. The elastic strain of a graphene monolayer has been predicted theoretically and also measured experimentally to be as high as 25% (refs 8,10,11), while that of bulk graphite rarely survives beyond 0.1% strain. Recently, a monolayer of molybdenum disulphide (MoS₂) was experimentally exfoliated and characterized. It demonstrated an effective in-plane strain of up to 11% (ref. 12), a direct bandgap of 1.9 eV under strain-free conditions^{13,14} and a more than 10,000-fold enhancement of its luminescence quantum yield compared to its bulk counterpart¹³. The high elastic strain limit should make it possible to control the electronic and optical properties of two-dimensional

materials through simple elastic strain engineering, which is often infeasible in their three-dimensional bulk phases. In addition, the lattice symmetry of MoS₂ also demonstrates a unique valley-selective circular dichroism^{15,16}.

Here, we illustrate theoretically and computationally that elastic strain is a viable agent for creating a continuously varying bandgap profile in an initially homogeneous, atomically thin membrane. As a proof of concept, an ‘artificial atom’ made of a nanoindented MoS₂ monolayer was investigated and predicted to be able to absorb a broad range of the solar spectrum from 2.0 eV to 1.1 eV as the biaxial strain increases from 0% to 9%. More importantly, the continuous spatial variation of electron and hole energies, together with the large exciton binding energy in the MoS₂ artificial atoms, makes it a unique solar energy funnel for conveying and concentrating the photoexcited charge carriers along the elastic strain gradient.

Introducing inhomogeneous elastic strain

When subjecting an atomically thin membrane to a simple external load, as shown in Fig. 1a, an inhomogeneous strain field can be created. The equilibrium geometry for a thin membrane is given by the Föppl–Hencky equation for membrane deformation under a stretching force at the boundaries only. For the geometry depicted in Fig. 1a, we have, for any line $\lambda(y)$, $h \int_{\lambda} dx \sigma_{\alpha} = f_{\alpha}$, where f_{α} is the stretching force on the boundary and h is the nominal membrane thickness. Owing to the force balance, the continuously narrowing membrane geometry can efficiently focus the tensile strain.

For the proposed device to function, inelastic strain relaxation as a result of dislocation plasticity or fracture must be avoided⁶. With a high-quality atomic membrane with minimal lattice defects, the edge lengths should also be minimized, as they are preferential sites for stress-aided defect nucleation¹⁷. We thus arrive at a setup similar to nanoindentation¹⁸, where a semiconducting membrane covers a circular hole on a substrate, with its rim clamped (Fig. 1b). A force probe is used to indent the suspended membrane, which will then deform towards a bottom contact. The stress gradient and hence the elastic strain gradient are maintained by the concentrated load setup with the stress scaling inversely with the radius:

¹International Center for Quantum Materials, School of Physics, Peking University, Beijing 100871, China, ²Department of Nuclear Science and Engineering and Department of Materials Science and Engineering, Massachusetts Institute of Technology, Cambridge, Massachusetts 02139, USA, ³State Key Laboratory for Mechanical Behavior of Materials and Frontier Institute of Science and Technology, Xi’an Jiaotong University, Xi’an, 710049, China; [†]These authors contributed equally to this work. *e-mail: liju@mit.edu

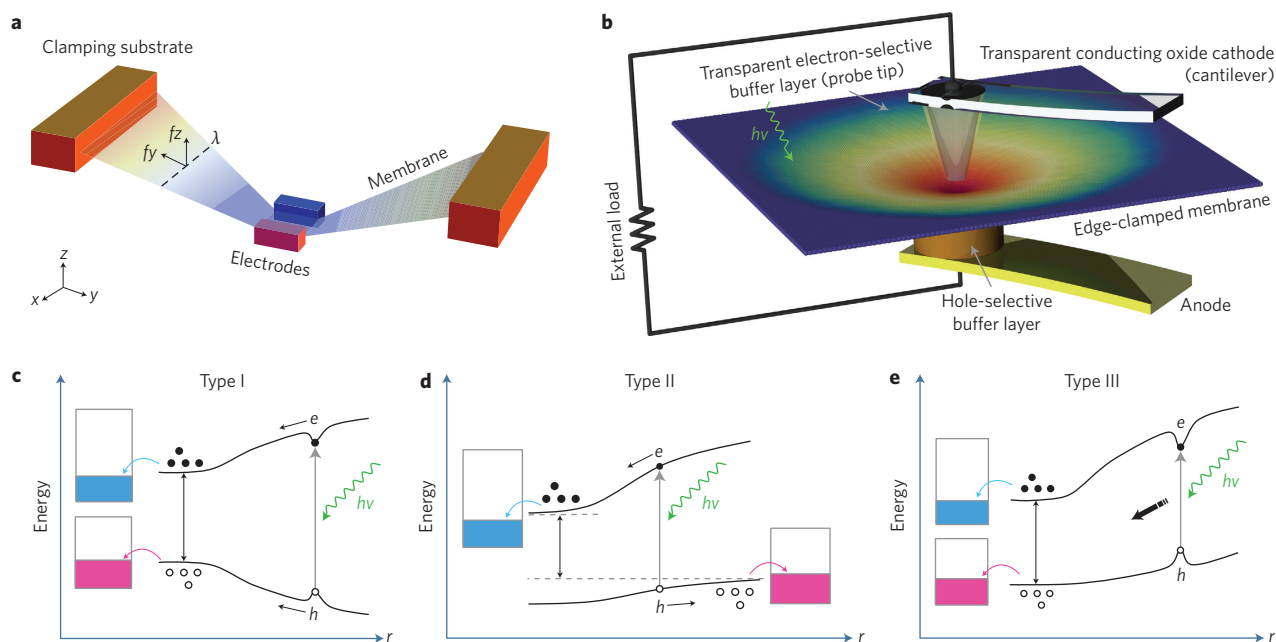


Figure 1 | Introducing inhomogeneous strain and classifying funnelling mechanisms. **a**, Schematic of an inhomogeneously strained membrane ribbon with varying width λ (dashed line). The two electrodes mechanically impose a vertical displacement on the central region of the membrane. Without the two electrodes, the equilibrium geometry of the membrane is flat. **b**, Schematic device setup for elastic strain-engineered artificial atom (not drawn to scale). Notice that although the bulk of the electrodes are metallic (for example, transparent conducting oxide), they are coated with semiconducting buffers to facilitate selective quasiparticle collection (detailed in the text). This setup completely removes the edges of the membrane ribbon in **a**, as these can serve as preferential sites for stress-aided defect nucleation. **c–e**, Three broad-spectrum solar energy funnelling mechanisms arising from a different band bending and exciton binding profile in the strain-engineered semiconducting membrane.

$\sigma_r \approx 1/r$ for $r < R$ (outer radius). Such a strain field resembles the potential field of a two-dimensional hydrogenic atom (but at a much larger length scale). It is in this sense that the strain-engineered atomic membrane can be regarded as a mesoscopic ‘artificial atom’ with electronic and optical properties that depend strongly on the strain and stress fields.

Broad-spectrum solar energy funnel

The connection between elastic strain and electronic structure in a strain-engineered artificial atom becomes apparent when the membrane is a semiconductor whose bandgap reflects a covalent bonding interaction. When stretched elastically, the covalent interaction generally weakens as the bonds lengthen, and consequently becomes a function of the imposed strain field. The stress is expected to exert significant modulation on the band energies and bandgap, analogous to band bending in a diode. The general principle here is to create a device with an electronic structure that has a continuous spatial variation due to an inhomogeneous strain field.

The scenario of continuous band bending leads us to propose the concept of a solar energy funnel. Based on the energy profiles of quasiparticles (that is, electrons and holes) and photoexcited states (that is, free electron–hole pairs or strongly bound excitons), three funnelling mechanisms are possible, as shown in Fig. 1c–e. In a Type I funnel, the energy level of photoexcited electrons continuously decreases towards the centre, while that of holes increases. Consequently, charge carriers are concentrated at the centre, as long as the lifetime of carriers is large enough for carrier migration before electron–hole recombination takes place. However, if both levels decrease with increasing strain, the result will depend on the strength of the Coulomb interaction between the quasiparticles, that is, the exciton binding energy. With weak exciton binding, electron–hole pairs will be separated by the built-in field and move in opposite directions, resulting in a Type II funnel. On the other hand, if the binding energy of an exciton is large enough to hold

the electron–hole pair together despite the built-in field, the decreasing exciton energy profile will drive the exciton to migrate towards the centre. A device based on this mechanism is classified as a Type III funnel. In all three types, the varying band/carrier energy leads to a funnelling effect. The strength of exciton binding energy determines whether Type II or III funnelling will operate in the device when the quasiparticle energy of both electron and hole decreases towards the centre of the membrane. A key advantage of such a strain-engineered device is that the performance of these devices can be adjusted to the lighting environment, as the optical bandgap is also continuously tunable.

Strain-dependent properties of MoS₂ monolayer

The structure of the MoS₂ monolayer is shown in the inset to Fig. 2d (Supplementary Fig. S1) and exhibits a remarkable trigonal prismatic geometry^{15,16,19}. On application of a biaxial strain, Poisson contraction²⁰ is expected. Owing to its hexagonal space group (*P6m2*) symmetry, the MoS₂ monolayer has isotropic in-plane elasticity, so the bandgap depends only on the two-dimensional hydrostatic strain invariant to the linear order. We therefore focus on the effect of biaxial strain on electronic structure. First-principles density functional theory^{21,22} (DFT) calculations (see Methods) indicate that both direct and indirect DFT bandgaps decrease (Fig. 2a,b), so a transition from direct bandgap to indirect bandgap occurs once the biaxial strain is applied. Other groups^{23,24} have recently reported a similar DFT bandgap reduction under biaxial tensile strain.

To acquire an accurate electronic band energy profile for the device design, we also performed many-body GW calculations^{25,26} (G, Green’s function; W, screened Coulomb interaction; see Methods). The strain-dependent bandgaps are shown in Fig. 2b, and the strain-dependent energy levels for an electron and hole at the K point in the first Brillouin zone are shown in Fig. 2d. As shown in Fig. 2b, the direct and indirect bandgaps calculated

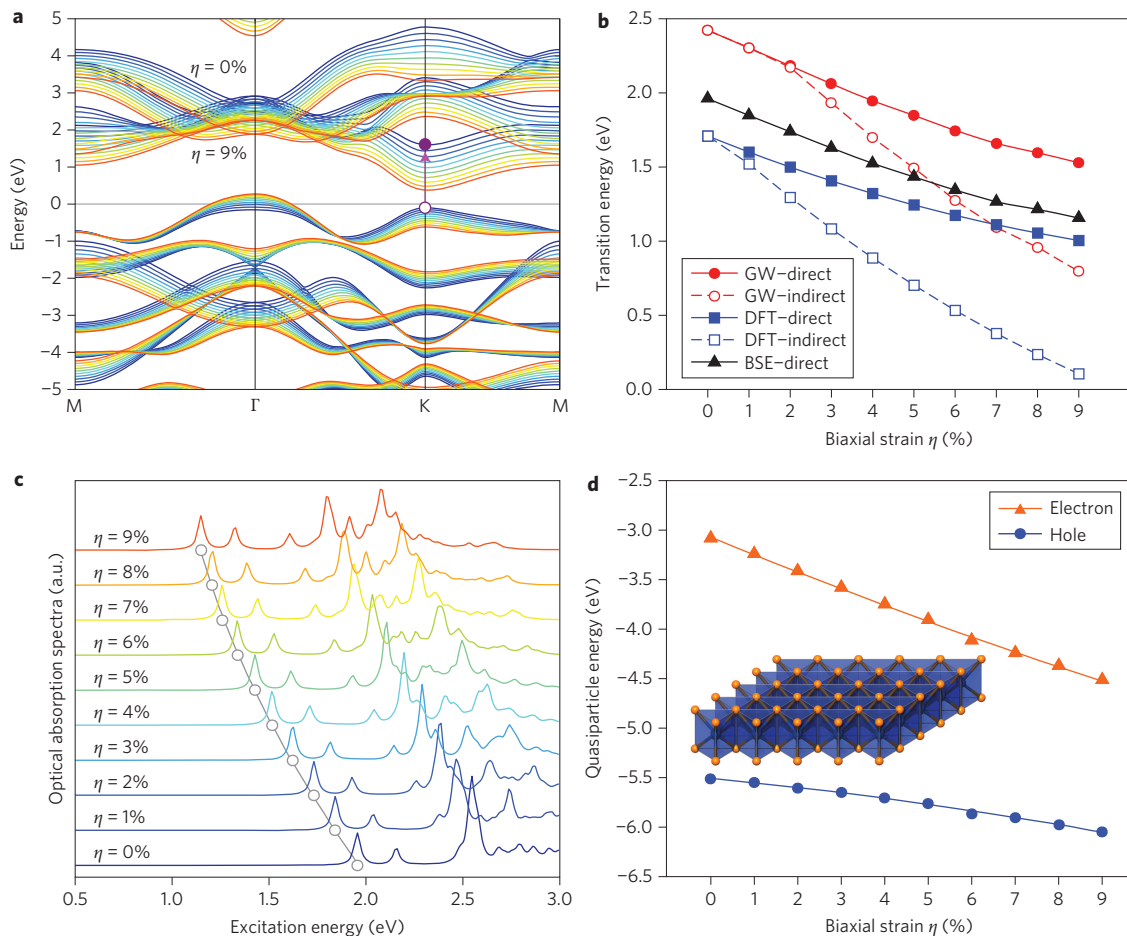


Figure 2 | Strain-dependent electronic and optical properties of MoS₂ monolayer. **a**, Electronic DFT band structure of monolayer MoS₂ under different biaxial strains from 0% (blue line) to 9% (red line). **b**, Direct and indirect bandgaps under different biaxial strains calculated using DFT and GW. The GW direct bandgap refers to the minimal direct transition energy. It is located at the K points of the hexagonal Brillouin zone, indicated by an arrow in **a**. The corresponding lowest optical excitation energy (black triangles) is calculated by BSE on top of GW quasiparticle energies with electron-hole Coulomb interaction included. **c**, Biaxial strain-dependent optical absorption spectra calculated by BSE. **d**, Biaxial strain-dependent GW quasiparticle energies for electrons and holes at the K point. Inset: atomic structure of MoS₂ monolayer.

from DFT and GW are indeed similar, except for a constant shift of 0.7 eV. Furthermore, the dielectric functions and electron energy loss spectrum of a MoS₂ monolayer are also predicted to undergo substantial changes under biaxial tensile strain (Supplementary Fig. S2).

The biaxial strain also modifies the absorption spectra and optical gap of the monolayer—the latter being another physical quantity important for device operation. As screening is generally reduced in a two-dimensional material, photoexcited quasiparticles in a MoS₂ monolayer are expected to experience stronger Coulomb attractions. We therefore go beyond the random-phase approximation by solving the Bethe–Salpeter equation (BSE)^{27,28} with GW quasiparticle energies. The calculated strain-dependent optical absorption spectra are displayed in Fig. 2c and show that the direct-to-indirect transition of the bandgap with biaxial strain does not affect the strength of the vertical optical absorption compared to the GW direct bandgap in Fig. 2b, BSE; it only shifts the whole spectrum to lower energy due to exciton binding. The lowest optical excitation in Fig. 2c originates from the doubly degenerate singlet excitons around the K points²⁹. The exciton energy of 2.0 eV at zero strain is in excellent agreement with the A peak at 1.9 eV measured using photoluminescence spectroscopy^{13,14} (the fine structure due to spin–orbit coupling discussed in ref. 29 is ignored here as it will not affect the main conclusion of strain-dependent electronic and optical energies). The excitation energy experiences substantial reduction when the strain is imposed,

decreasing to 1.1 eV at 9% biaxial strain. We then arrive at a roughly constant exciton binding energy of 0.5 eV from 0% to 9% biaxial strain. Such large constant exciton binding energy together with the reduced quasiparticle energies (Fig. 2d) makes the strain-engineered artificial MoS₂ atom a Type III solar energy funnel.

Exciton wavefunctions for the lowest excitation under zero strain are displayed in Supplementary Fig. S3. The hole state is dominated by $d_{x^2-y^2}$ and d_{xy} orbitals of molybdenum atoms and p_x and p_y orbitals of sulphur atoms, and the electron state is dominated by d_{z^2} orbitals of molybdenum atoms. The large exciton radius (~2 nm) and exciton binding energy (~0.5 eV) indicate a mixed Frenkel–Wannier–Mott exciton character. This arises from the reduced screening in two-dimensional atomically thin materials and thus stronger Coulomb attraction between electrons and holes upon photoexcitation.

Nanoindented MoS₂ monolayer as artificial atoms

To compute the morphology of the MoS₂ monolayer in the proposed device, we used a bicontinuum finite-element simulation³⁰, with a force field parameterized in the Tersoff potential form³¹ (see Supplementary Information). This coarse-grained force field method yields essentially the same membrane morphology as the analytical solution to the Föppl–Hencky equations³² (Supplementary Fig. S4). The computed morphology of the deformed membrane shows characteristic scale invariance; that is,

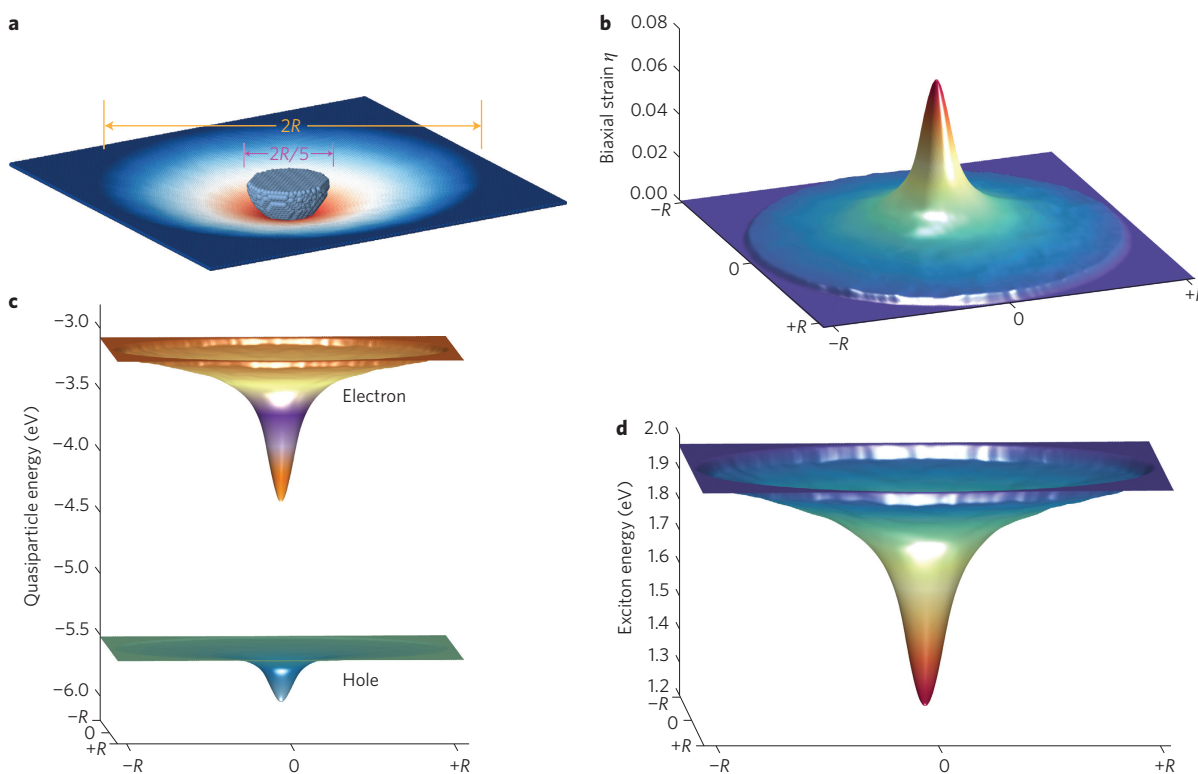


Figure 3 | Structural and physical properties of nanoindented MoS₂ monolayer. **a**, Atomic structure of circular MoS₂ membrane under indentation with a maximum vertical displacement of $R/5$ (R , circular membrane radius). **b**, Biaxial strain in the MoS₂ membrane calculated from the least-square atomic strain tensor. **c,d**, Corresponding local electron and hole energy profile (**c**) and local exciton energy profile (**d**). These are directly mapped from the profiles of homogeneously biaxial strained MoS₂ monolayer against the biaxial invariants of the strain tensor in inhomogeneously deformed MoS₂ membrane under indentation.

w/R as a function of r/R is nearly independent of R for $R > 100$ Å, where w is the vertical displacement at radius r . In practice, a force probe with a rounded tip (Fig. 1b) can be used to avoid stress singularity near the centre. A relaxed atomic structure of nanoindented MoS₂ membrane is shown in Fig. 3a, demonstrating a maximum vertical displacement of $Z = R/5$. The displacement increases gradually towards the centre of the membrane. This is expected as the boundary conditions (edge clamping and central indenting) have cylindrical symmetry, and the hexagonal lattice implies the same symmetry in the Young's modulus and Poisson ratio³³. The computed biaxial field is visualized in Fig. 3b (see Supplementary Information for calculation details). Right at the clamped rim of the suspended membrane, the biaxial strain has a small abrupt increase due to the boundary used in the simulation. As one moves inwards, the strain increases quickly, corresponding to the increase in radial stress. Because the tip of the force probe is rounded, the elastic strain does not diverge near the centre of the membrane.

With the computed strain pattern shown in Fig. 3b, we can map out the energy profiles of electronic and optical excitations on the membrane in a semiclassical sense, using those of the MoS₂ monolayer under different amounts of homogeneous biaxial strain, as presented above. The mapped band edges of electrons and holes and the energy profile of excitons for the representative membrane are shown in Fig. 3c and d, respectively. Both valence and conduction band edges are shifted downward from the rim to the centre. At the region with slowly varying strain, there is a large plateau where the positions of the band edges are almost constant, with an area occupying almost two-thirds of the circular region. The spatial variation of exciton energy in the membrane, except for the sign difference, is very similar to the strain profile, as the total

exciton energy changes almost linearly with respect to the applied biaxial strain (Fig. 2b).

The size of Type III solar energy funnel device is essentially constrained by the exciton drift length, beyond which radiative recombination will dominate and prevent the exciton from reaching the electrodes at the centre. The exciton drift length³⁴ can be estimated by

$$l_{\text{drift}} = \langle v \rangle_{\text{drift}} \tau_{1/2} = \frac{\nabla E_{\text{exc}}}{m_{\text{exc}}} \tau_{\text{dephase}} \tau_{1/2} \quad (1)$$

where $\tau_{1/2}$ is the exciton lifetime and $\langle v \rangle_{\text{drift}}$ is the average drift velocity. The latter is then estimated by the acceleration of the exciton due to the exciton energy gradient ∇E_{exc} within phase relaxation time $\langle v \rangle_{\text{drift}}$. The exciton mass is denoted m_{exc} . As we would like to have most excitons collected at the centre of the membrane, the radius of the membrane should be set to the drift length, that is, $R = l_{\text{drift}}$. Hence, the spatial gradient of the exciton energy ∇E_{exc} can be approximated by $\Delta E_{\text{exc}}/R$. We therefore have an effective membrane radius,

$$R = \sqrt{m_{\text{exc}}^{-1} \Delta E_{\text{exc}} \tau_{\text{dephase}} \tau_{1/2}} \quad (2)$$

In the plateau region, the energy variation ΔE_{exc} is ~ 0.1 eV. As we do not know exciton mass m_{exc} and phase relaxation time τ_{dephase} , we approximate them by the electron rest mass m_e and ~ 5 ps in GaAs³⁵, respectively. Fortunately, the exciton lifetime $\tau_{1/2}$ of a MoS₂ monolayer has recently been measured³⁶, with a fast photoluminescence decay component of 5 ps at temperatures of ~ 4.5 –150 K and a slow decay component of 100 ps at 270 K.

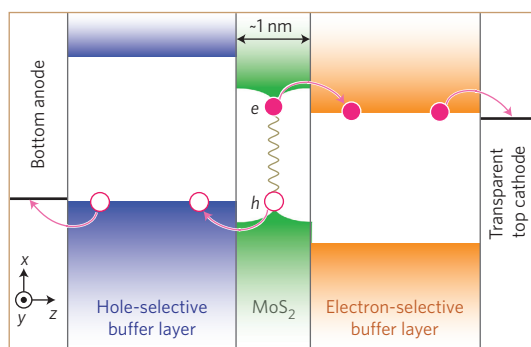


Figure 4 | Schematic of charge extraction near the centre of the atomic membrane. The atomic membrane lies on the x - y plane, and the indentation is along the z -direction. Two semiconducting buffer layers between the MoS_2 monolayer and the two electrodes serve as electron-selective and hole-selective transporters due to their specific band alignment with respect to the MoS_2 monolayer. These two buffer layers are thick enough to make direct tunnelling negligible. In addition, a transparent conducting oxide is used as the cathode so as not to block the incoming light from the top.

The estimated radius of the atomic membrane is then ~ 660 nm and $3 \mu\text{m}$ for the fast and slow decay components, respectively.

Compared to the above characteristic size of the membrane, the exciton radius of 2 nm (Supplementary Fig. S3) is indeed much smaller, meaning that the strain profile continuously and smoothly varies over a length scale comparable to the exciton size in the region of interest. The continuum strain mapping procedure is therefore justified. It is now entirely plausible that upon excitation from the ground state, the excitons will be swept by the strain-induced potential gradient and funnelled toward the centre. As both hole and electron carriers are bound in the same direction, we expect that the membrane will stay essentially charge neutral during device operation. This is advantageous, as charging might otherwise significantly reduce the efficiency of the carrier funneling. The final charge separation and harvesting of solar energy can be achieved by contacting an electron-collecting transparent semiconductor on top of the arrangement and a hole-collecting semiconductor at the bottom (Fig. 1b), with appropriate band-edge alignments to ensure one-way electron/hole flow, as in standard photovoltaic technology. As the electron-hole pairs represent energetic excited states, the membrane device works like a battery with an electropotential $\Delta V_{\text{ext}} < \Delta V_{\text{int}}$.

Discussion

What we have created in the MoS_2 membrane with the elastic strain pattern is a continuous bending of the energy levels of electrons, holes and excitons, similar to that in a photodiode, except that the photoexcited electron-hole pairs in MoS_2 are strongly bound excitons. When an electron-hole pair is generated in the plateau region following light absorption, the semiclassical potential for the quasiparticles exerts forces on the electron and hole in opposite directions. However, the large exciton binding energy will force the electron-hole pair to hold together like a molecule (despite a small polarization) and migrate towards the centre of the membrane. This is different from the case of a photodiode, where electron-hole pairs quickly dissociate, with the electrons and holes then migrating in opposite directions.

Although not central to the proposed photocarrier funneling effect, the eventual collection of solar energy is also critical. To efficiently extract charge carriers from the centre, the device design shown in the schematic in Fig. 1b was proposed, with a band alignment as shown in Fig. 4. Such a structure is similar to that of organic photovoltaic cells^{37,38}. The charge extraction process is accomplished with two carrier-collecting contacts, one of which is the

indenter itself, and the other is located beneath the indented MoS_2 membrane. The bulk of the electrodes are made of transparent conducting oxide to maximize illumination of the membrane. Key to the design are two semiconducting buffer layers, which cover the electrodes and come into direct contact with the MoS_2 monolayer. The role of these buffer layers is to selectively admit one type of charge carrier (electron or hole) while blocking the other. The carrier selectivity of these buffers arises from band alignment (detailed in Fig. 4) and follows the standard principle from photovoltaics. The nanoindebiter tip in Fig. 1b should therefore be made of, or coated with, transparent semiconductors with selected band edges. This is particularly important when building a functional funnel device such as that in Fig. 1b, because the buffer layers can help suppress direct tunnelling of carriers between anode and cathode and allow for efficient extraction of charge carriers. A layered patterning scheme is also proposed in Supplementary Fig. S6 to achieve arrays of strain-engineered artificial atoms.

The concept of a solar energy funnel achieved by engineering the electronic band energy and optical bandgap is not entirely new, and has been demonstrated experimentally in several nanostructures with graded gaps, including layer-by-layer assembled CdTe nanocrystals of different sizes³⁹ and core-shell and corrugated carbon nanotube filaments⁴⁰. Here, however, we have explored an alternative approach by generating continuously varying electronic band energy and optical bandgap in two-dimensional atomically thin membranes, by means of inhomogeneous elastic strain engineering within a single crystalline material. We would like to emphasize that it is the varying profile of band energy that leads to the direct funneling effect, while the strength of the exciton binding energy determines whether a Type II or Type III funnel device is created. The present approach is enabled by recent rapid advances in two-dimensional atomically thin sheets such as graphene, hexagonal boron-nitride, MoS_2 monolayer and so on. All of these have been exfoliated experimentally and characterized to have very high elastic strain limits. In addition, MoS_2 has some other attractive properties such as high thermal stability and chemical inertness. We therefore expect that the proposed funnel device can be verified by experiments in the near future.

In closing, we would like to make three remarks. First, photovoltaic conversion and the solar energy funnel are not the only applications of the proposed artificial atom. For example, without the electrodes, the excitons concentrated at the centre will be relaxed through radiative recombination, resulting in stronger luminescence near the centre of the membrane. This may be useful for exciton lasing, if an appropriate resonator design is devised⁴¹. The unique feature of the device, as exemplified above, is its mechanical tunability; the frequency and intensity of the emission can be tuned continuously by varying the applied strain to the atomic membrane. Second, the concept of a strain-engineered artificial atom may work with many other atomically thin sheets, including GaS, GaSe, GaTe, MX_2 -type dichalcogenides ($M=\text{Mo, Nb, Ni, Sn, Ti, Ta, Pt, V, W, Hf}$ and so on, and $X=\text{S, Se, Te}$), M_2X_3 -type trichalcogenides ($M=\text{As, Bi, Sb}$ and so on, and $X=\text{S, Se, Te}$), MPX_3 ($X=\text{S, Se}$), MAX_3 ($A=\text{Si, Ge}$, and $X=\text{S, Se, Te}$), and alloy sheets like $\text{M}_x\text{M}'_{1-x}\text{S}_2$. It can also be applied to other thin membranes based on conventional materials, such as a silicon nanomembrane⁴², which can sustain a significant tensile strain of a few percent. This level of tension is sufficient to induce the proposed funneling effect, even though the driving force is still not as large as in maximally indented atomic sheets. Finally, although we illustrate the application of the elastically deformed membrane semiconductor as a solar energy concentrator, we would also like to emphasize the more general notion of it being a tunable artificial atom. Each deformable membrane should have its own characteristic excitations (electronic and electromagnetic). Upon juxtaposition, they will interact electronically

and optically. It is our hope, then, that complex superlattice arrays of these artificial atoms can be built on a whole membrane, the properties of which will be tuned at the level of the fundamental 'atomic' building blocks by strain engineering.

Methods

Ground-state properties of MoS₂ monolayer. The ground-state atomic structure of MoS₂ monolayer under different biaxial strains was first assessed by DFT^{21,22} calculations. These were carried out using the Vienna Ab initio Simulation Package (VASP) with a plane wave basis^{43,44} and the projector-augmented wave method⁴⁵. Exchange-correlation functionals in a Perdew–Berke–Ernzerhof (PBE) form⁴⁶ within the generalized-gradient approximation (GGA)^{47,48} were used in all DFT calculations. We adopted the Monkhorst–Pack scheme⁴⁹ of k-point sampling for zone integration, and selected the number of k-points to achieve a convergence in total energy within ~1 meV/atom. The total energy of each optimized structure was calculated again with the more accurate tetrahedron zone summation with Blöchl correction⁵⁰. A qualitative electronic band structure for different biaxial tensile strain was also obtained from DFT–PBE calculations.

Excited-state properties of MoS₂ monolayer. Two physical quantities related to this design of solar energy funnel are the electronic excitation energy (quasiparticle band energy for electron and hole) and optical excitation energy (exciton energy). However, neither of these can be obtained accurately from DFT Kohn–Sham eigen energies using the GGA exchange–correlation function. We therefore computed quasiparticle energies for electrons and holes using many-body perturbation theory calculations within Hedin's G₀W₀ approximation^{25,26}, while the optical absorption spectra and exciton energies were further obtained by solving a Bethe–Salpeter equation^{27,28} on top of G₀W₀ quasiparticle energies within the Tamm–Dancoff approximation, which explicitly takes into account Coulomb interactions between quasi-electrons and quasi-holes. Here, an energy cutoff of 350 eV and Monkhorst–Pack k-point sampling of 18 × 18 × 1 were chosen. Both GW and BSE calculations require much more computational effort and memory storage than DFT calculations, because the GW method needs to evaluate frequency-dependent non-local self-energy and the BSE method is essentially solving two-particle Green's function, whereas DFT with GGA functions is intrinsically local and frequency-independent. Because an exciton corresponds to the excitation of electron–hole pairs, its wavefunction is a six-dimensional quantity, $\Psi(\mathbf{r}_e, \mathbf{r}_h) = \sum_{\mathbf{k}, \nu} A_{\nu\mathbf{k}} \phi_{\mathbf{k}}(\mathbf{r}_e) \phi_{\mathbf{k}}^*(\mathbf{r}_h)$, where $\phi_{\mathbf{k}}(\mathbf{r}_e)$ and $\phi_{\mathbf{k}}^*(\mathbf{r}_h)$ are electron and hole wavefunctions. We have reconstructed exciton wavefunctions and plotted out the corresponding electron (hole) wavefunction by holding its counterpart hole (electron) at a specific location (Supplementary Fig. S3). Spin–orbit coupling is not included as it will not affect the main conclusion of strain-dependent electronic and optical bandgaps of MoS₂ monolayer.

Geometry of the MoS₂ membrane under nanoindentation. Owing to the large size of the atomic membrane under consideration here, it is unrealistic for us to relax the nanoindented membrane by first-principles DFT calculation directly. We therefore fitted a set of Tersoff potential parameters for MoS₂, and then performed force-field calculations to obtain the geometry of the MoS₂ membrane under indentation. More details are provided in the Supplementary Information.

Received 13 March 2012; accepted 17 October 2012;
published online 25 November 2012

References

- Shockley, W. & Queisser, H. J. Detailed balance limit of efficiency of p–n junction solar cells. *J. Appl. Phys.* **32**, 510–519 (1961).
- Henry, B. R. & Greenlay, W. R. A. Detailed features in the local mode overtone bands of ethane, neopentane, tetramethylbutane, and hexamethylbenzene. *J. Chem. Phys.* **72**, 5516–5524 (1980).
- De Vos, A. Detailed balance limit of the efficiency of tandem solar-cells. *J. Phys. D* **13**, 839–846 (1980).
- Kang, Z., Tsang, C. H. A., Wong, N.-B., Zhang, Z. & Lee, S.-T. Silicon quantum dots: a general photocatalyst for reduction, decomposition, and selective oxidation reactions. *J. Am. Chem. Soc.* **129**, 12090–12091 (2007).
- McDonald, S. A. *et al.* Solution-processed PbS quantum dot infrared photodetectors and photovoltaics. *Nature Mater.* **4**, 138–142 (2005).
- Zhu, T. & Li, J. Ultra-strength materials. *Prog. Mater. Sci.* **55**, 710–757 (2010).
- Zhu, T., Li, J., Ogata, S. & Yip, S. Mechanics of ultra-strength materials. *MRS Bull.* **34**, 167–172 (2009).
- Lee, C., Wei, X. D., Kysar, J. W. & Hone, J. Measurement of the elastic properties and intrinsic strength of monolayer graphene. *Science* **321**, 385–388 (2008).
- Novoselov, K. S. *et al.* Two-dimensional atomic crystals. *Proc. Natl Acad. Sci. USA* **102**, 10451–10453 (2005).
- Liu, F., Ming, P. M. & Li, J. *Ab initio* calculation of ideal strength and phonon instability of graphene under tension. *Phys. Rev. B* **76**, 064120 (2007).
- Feng, J. *et al.* Patterning of graphene. *Nanoscale* **4**, 4883–4899 (2012).
- Bertolazzi, S., Brivio, J. & Kis, A. Stretching and breaking of ultrathin MoS₂. *ACS Nano* **5**, 9703–9709 (2011).
- Mak, K. F., Lee, C., Hone, J., Shan, J. & Heinz, T. F. Atomically thin MoS₂: a new direct-gap semiconductor. *Phys. Rev. Lett.* **105**, 136805 (2010).
- Splendiani, A. *et al.* Emerging photoluminescence in monolayer MoS₂. *Nano Lett.* **10**, 1271–1275 (2010).
- Cao, T. *et al.* Valley-selective circular dichroism of monolayer molybdenum disulphide. *Nature Commun.* **3**, 887 (2012).
- Xiao, D., Liu, G.-B., Feng, W., Xu, X. & Yao, W. Coupled spin and valley physics in monolayers of MoS₂ and other group-VI dichalcogenides. *Phys. Rev. Lett.* **108**, 196802 (2012).
- Li, J. The mechanics and physics of defect nucleation. *MRS Bull.* **32**, 151–159 (2007).
- Li, J., van Vliet, K. J., Zhu, T., Yip, S. & Suresh, S. Atomistic mechanisms governing elastic limit and incipient plasticity in crystals. *Nature* **418**, 307–310 (2002).
- Hoffmann, R., Howell, J. M. & Rossi, A. R. Biccapped tetrahedral, trigonal prismatic, and octahedral alternatives in main and transition group six-coordination. *J. Am. Chem. Soc.* **98**, 2484–2492 (1976).
- Landau, L. D., Lifshits, E. M., Kosevich, A. M. & Pitaevskii, L. P. *Theory of Elasticity* 3rd English edn 12 (Pergamon Press, 1986).
- Hohenberg, P. & Kohn, W. Inhomogeneous electron gas. *Phys. Rev. B* **136**, B864–B871 (1964).
- Kohn, W. & Sham, L. J. Self-consistent equations including exchange and correlation effects. *Phys. Rev.* **140**, A1133–A1138 (1965).
- Scalise, E., Houssa, M., Pourtois, G., Afanas'ev, V. V. & Stesmans, A. Strain-induced semiconductor to metal transition in the two-dimensional honeycomb structure of MoS₂. *Nano Res.* **5**, 43–48 (2012).
- Yun, W. S., Han, S. W., Hong, S. C., Kim, I. G. & Lee, J. D. Thickness and strain effects on electronic structures of transition metal dichalcogenides: 2H–MX₂ semiconductors (M=Mo, W; X=S, Se, Te). *Phys. Rev. B* **85**, 033305 (2012).
- Hedin, L. New method for calculating one-particle Green's function with application to electron-gas problem. *Phys. Rev.* **139**, A796–A823 (1965).
- Hybertsen, M. S. & Louie, S. G. First-principles theory of quasiparticles: calculation of band-gaps in semiconductors and insulators. *Phys. Rev. Lett.* **55**, 1418–1421 (1985).
- Salpeter, E. E. & Bethe, H. A. A relativistic equation for bound-state problems. *Phys. Rev.* **84**, 1232–1242 (1951).
- Onida, G., Reining, L. & Rubio, A. Electronic excitations: density-functional versus many-body Green's-function approaches. *Rev. Mod. Phys.* **74**, 601–659 (2002).
- Ramasubramaniam, A. Large excitonic effects in monolayers of molybdenum and tungsten dichalcogenides. *Phys. Rev. B* **86**, 115409 (2012).
- Nisoli, C., Lammert, P. E., Mockensturm, E. & Crespi, V. H. Carbon nanostructures as an electromechanical bicontinuum. *Phys. Rev. Lett.* **99**, 045501 (2007).
- Tersoff, J. New empirical-approach for the structure and energy of covalent systems. *Phys. Rev. B* **37**, 6991–7000 (1988).
- Jin, C. R. Large deflection of circular membrane under concentrated force. *Appl. Math. Mech. Engl.* **29**, 889–896 (2008).
- Nye, J. F. *Physical Properties of Crystals: Their Representation by Tensors and Matrices* 20–30 (Clarendon Press, 1985).
- Shimizu, M. Long-range pair transport in graded band gap and its applications. *J. Lumin.* **119**, 51–54 (2006).
- Honold, A., Schultheis, L., Kuhl, J. & Tu, C. W. Collision broadening of two-dimensional excitons in GaAs single quantum well. *Phys. Rev. B* **40**, 6442–6445 (1989).
- Korn, T., Heydrich, S., Hirmer, M., Schmutzler, J. & Schuller, C. Low-temperature photocarrier dynamics in monolayer MoS₂. *Appl. Phys. Lett.* **99**, 102109 (2011).
- Kim, J. Y. *et al.* New architecture for high-efficiency polymer photovoltaic cells using solution-based titanium oxide as an optical spacer. *Adv. Mater.* **18**, 572–576 (2006).
- Li, G., Zhu, R. & Yang, Y. Polymer solar cells. *Nature Photon.* **6**, 153–161 (2012).
- Franzl, T., Klar, T. A., Schietinger, S., Rogach, A. L. & Feldmann, J. Exciton recycling in graded gap nanocrystal structures. *Nano Lett.* **4**, 1599–1603 (2004).
- Han, J. H. *et al.* Exciton antennas and concentrators from core–shell and corrugated carbon nanotube filaments of homogeneous composition. *Nature Mater.* **9**, 833–839 (2010).
- Watanabe, K., Taniguchi, T. & Kanda, H. Direct-bandgap properties and evidence for ultraviolet lasing of hexagonal boron nitride single crystal. *Nature Mater.* **3**, 404–409 (2004).
- Lagally, M. G. Silicon nanomembranes. *MRS Bull.* **32**, 57–63 (2007).
- Kresse, G. & Furthmüller, J. Efficiency of *ab-initio* total energy calculations for metals and semiconductors using a plane-wave basis set. *Comput. Mater. Sci.* **6**, 15–50 (1996).
- Kresse, G. & Furthmüller, J. Efficient iterative schemes for *ab initio* total-energy calculations using a plane-wave basis set. *Phys. Rev. B* **54**, 11169–11186 (1996).
- Blöchl, P. E. Projector augmented-wave method. *Phys. Rev. B* **50**, 17953–17979 (1994).

46. Perdew, J. P., Burke, K. & Ernzerhof, M. Generalized gradient approximation made simple. *Phys. Rev. Lett.* **77**, 3865–3868 (1996).
47. Langreth, D. C. & Mehl, M. J. Beyond the local-density approximation in calculations of ground-state electronic-properties. *Phys. Rev. B* **28**, 1809–1834 (1983).
48. Becke, A. D. Density-functional exchange-energy approximation with correct asymptotic-behavior. *Phys. Rev. A* **38**, 3098–3100 (1988).
49. Monkhorst, H. J. & Pack, J. D. Special points for Brillouin-zone integrations. *Phys. Rev. B* **13**, 5188–5192 (1976).
50. Blöchl, P. E., Jepsen, O. & Andersen, O. K. Improved tetrahedron method for Brillouin-zone integrations. *Phys. Rev. B* **49**, 16223–16233 (1994).

Acknowledgements

The authors appreciate helpful discussions with S.G. Johnson and M. Loncar, and acknowledge support from the NSF (DMR-1120901) and AFOSR (FA9550-08-1-0325),

as well as NSFC Project 11174009 and 973 Programs of China (2010CB631003, 2011CBA00109, 2012CB619402, 2013CB921900).

Author contributions

J.L. designed the project. J.F., X.F.Q. and C.W.H. carried out the calculations and the modelling. J.F., X.F.Q. and J.L. wrote the paper. All authors contributed to discussions of the results.

Additional information

Supplementary information is available in the online version of the paper. Reprints and permission information is available online at <http://www.nature.com/reprints>. Correspondence and requests for materials should be addressed to J.L.

Competing financial interests

The authors declare no competing financial interests.

Supplementary Information

Strain-engineered artificial atom as a broad-spectrum solar energy funnel

Ji Feng^{1,†}, Xiaofeng Qian^{2,†}, Cheng-Wei Huang² and Ju Li^{2,3,*}

¹ International Center for Quantum Materials, School of Physics, Peking University, Beijing 100871, China

² Department of Nuclear Science and Engineering and Department of Materials Science and Engineering, Massachusetts Institute of Technology, Cambridge, Massachusetts 02139, USA

³ State Key Laboratory for Mechanical Behavior of Materials and Frontier Institute of Science and Technology, Xi'an Jiaotong University, Xi'an, 710049, China

†These authors contributed equally to this work.

*Correspondence and requests for materials should be addressed to J.L. (email: lijul@mit.edu).

A. Inhomogeneous elastic strain in atomically thin membrane

When subjecting an atomically thin membrane to a simple external load as shown in [Fig. 1a](#) of the paper, an inhomogeneous strain field is created. The equilibrium geometry at the thin membrane limit is given by the Föppl-Hencky equation for a membrane deformation under stretching force only at the boundaries,

$$\sigma_{\alpha\beta} \frac{\partial^2 w}{\partial \alpha \partial \beta} = 0, \quad \frac{\partial \sigma_{\alpha\beta}}{\partial \beta} = 0 \quad (\text{S1})$$

where $\alpha, \beta = x, y$, w is the displacement along z -direction, $\sigma_{\alpha\beta}$ the stress tensor, and the pressure differential across the membrane is taken to be zero. The first and second equations express the

force balances along the z -direction and x - y plane, respectively. For the geometry depicted in Fig. 1a, we have for any line $\lambda(y)$, $h \int_{\lambda} dx \sigma_{\alpha} = f_{\alpha}$, where f_{α} is the stretching force on the boundary and h is nominal membrane thickness. Apparently, the average tensile stress in y -direction along line $\lambda(y)$ is

$$\bar{\sigma}_{\alpha} = \frac{|f_{\alpha}|}{h\lambda(y)}. \quad (\text{S2})$$

Thus, a continuously narrowing membrane geometry can efficiently focus the stress and the tensile strain. For a simple concentric geometry, the width w scales as r^{-1} , where $r=(x^2+y^2)^{1/2}$, so the elastic strain and strain-controlled properties (e.g. band gap) would also scale as r^{-1} .

B. Ground-state atomic and electronic structure of monolayer MoS₂

MoS₂ belongs to a family of low-dimensional semiconductors, the transition metal dichalcogenides MX₂ (X = S, Se). The structure of MoS₂ monolayer is shown in Fig. S1, where Mo atom sits in the cage formed by six sulfur atoms, forming a remarkable trigonal prismatic geometry^{1,2}. Crystal field splitting in such geometry determines its electronic structure, resulting in the states near the band gap largely residing on Mo atoms. This is clearly seen from electronic density of states (DOS) (Fig. S1) obtained from first-principles density-functional theory^{3,4} (DFT) calculations. Owing to its hexagonal space group ($P\bar{6}m2$) symmetry, MoS₂ monolayer has isotropic in-plane elasticity, so the band gap depends only on the hydrostatic strain invariant in 2D (i.e., biaxial strain), $\eta_{\text{hydro}} = (\eta_{xx} + \eta_{yy})/2$, in the linear order. We therefore focus on the effect of biaxial strain on the electronic and optical properties of MoS₂ monolayer in the main text.

However, it is known that DFT using local density approximation or generalized gradient approximation of exchange-correlation functional usually underestimates by 30%-50% the true

quasiparticle band gap. The DFT band structure (Fig. 2a) and DOS (Fig. S1c) only provide qualitative information of electronic structure of monolayer MoS₂. We thus have performed quasiparticle GW calculations for electron and hole energy levels and solved Bethe-Salpeter equation (BSE) for optical excitation energy and absorption spectrum. These two quantities together with the nonlinear strain map are the key physical parameters used in our device design.

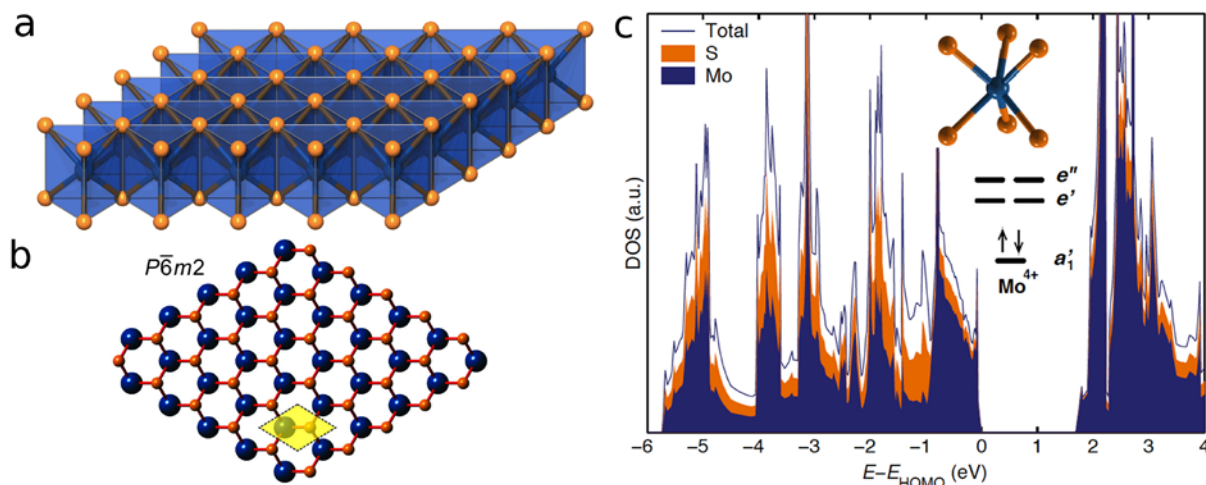


Figure S1 | Structure of monolayer MoS₂ viewed from (a) side and (b) top. (c) Electronic DOS of MoS₂ monolayer from DFT calculations, with projection onto Mo and S atoms. Inset: the local coordination of a Mo atom and the crystal-field splitting of its d -orbitals at the Brillouin zone centre.

C. Strain-dependent dielectric functions and electron energy loss spectrum of monolayer MoS₂

Below we report strain-dependent real ϵ_1 and imaginary ϵ_2 part of dielectric functions and electron energy loss spectrum (EELS) of monolayer MoS₂ for light polarized parallel to the monolayer surface. They are computed using the density-functional perturbation theory within the random-phase approximation. The results are shown in Fig. S2. We can see that all three

optical properties are found to be altered significantly under biaxial strain, which could be important for designing 2D photonic crystal using arrays of strain-engineered atomic membranes.

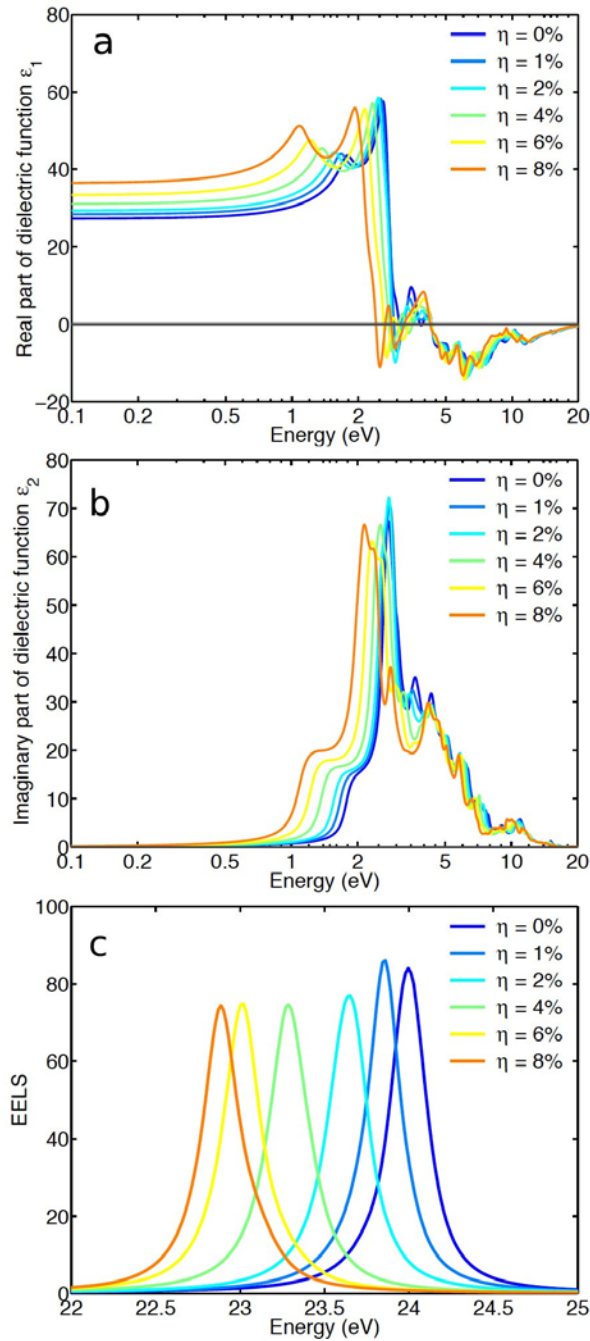


Figure S2 | Strain-dependent real (ϵ_1) and imaginary (ϵ_2) part of dielectric functions and electron energy loss spectrum of monolayer MoS₂ for light polarized parallel to the monolayer surface.

D. Exciton wavefunction in MoS₂ monolayer

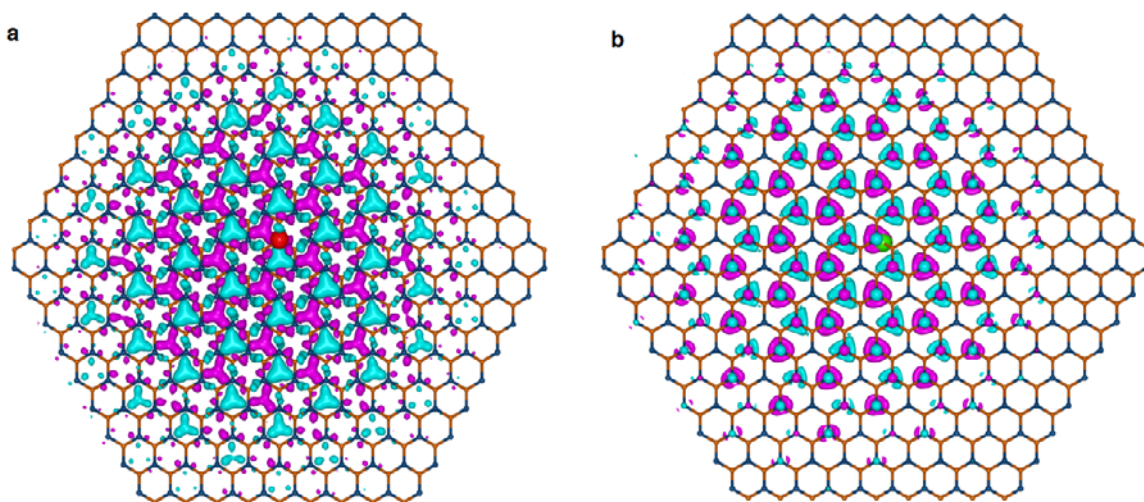


Figure S3 | The lowest exciton wavefunction in the unstrained MoS₂ monolayer. Its hole amplitude is shown in (a) with electron fixed at the centre (red dot), and its electron amplitude is shown in (b) with hole fixed at the centre (green dot). The magenta and cyan isosurfaces correspond to plus and minus sign, respectively, of the real part of amplitudes.

E. Coarse-grained force-field calculation

Before computing the morphology of MoS₂ monolayer under the proposed experimental setup, we note the following. First, the shape of circular, elastically isotropic membrane is well described by the Föppl-Hencky equation in the continuum limit. The hexagonal symmetry ($3/m$ class) of MoS₂ monolayer indicates that its Young's modulus and Poisson's ratio are isotropic in the plane. The only material properties entering the Föppl-Hencky are the Young's modulus (E) and the Poisson ratio (ν)^{5,6}. Second, the bipartite lattice of MoS₂ monolayer renders its mechanical deformation amenable to a bicontinuum treatment⁷. Therefore, we choose the Tersoff's force field that has a three-body angular term,⁸ with which a graphene-like structure is stable. The pair of S atoms occupying each site on the honeycomb net is treated as one particle. Further, we ignore the mass difference between the Mo and S-pair sites, which is appropriate

when only static morphology is sought. We also assume the variation of the potential corresponding to bending modes Mo-S-Mo and S-Mo-S are identical. Again, this is justified as only Young’s modulus and Poisson’s ratio determine the static response to an external stress⁵⁻⁷. Although Föppl-Hencky equation for circular membrane under a central load does entail the possibility of wrinkling instability⁶, we have not seen wrinkle formation in the membrane up to the point of membrane rupture in our simulations.

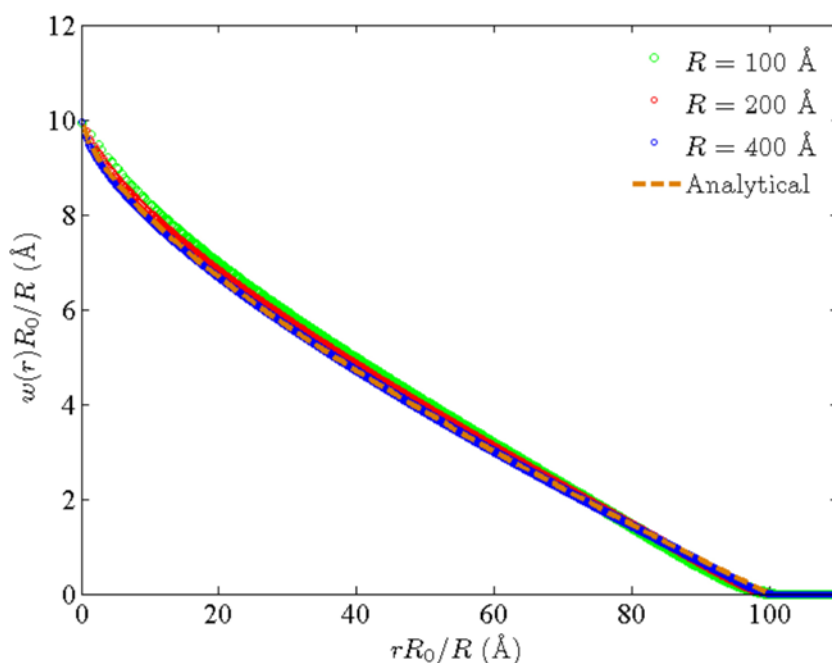


Figure S4 | Comparison between the membrane geometry computed from the coarse-grained force-field calculation and the exact results. Here, the vertical displacement $w(r)$ and the radius r are both scaled by R_0/R , where $R_0 = 100 \text{ \AA}$ and R is the radius of the current simulation in \AA .

We started with the Tersoff potential⁸ for carbon, and found that the only modifications we needed were, following the same notations in Ref. 8:

$$A(\text{MoS}_2) = 0.1833 \times A(\text{carbon}) = 255.44688 \text{ eV} \tag{S3}$$

$$B(\text{MoS}_2) = 0.1833 \times B(\text{carbon}) = 63.55011 \text{ eV}$$

where A and B appear in Eq. 3 of Ref. 8, and

$$d(\text{MoS}_2) = 0.84 \times d(\text{carbon}) = 3.652656 \text{ (dimensionless)} \quad (\text{S4})$$

where d is the angular term (Eq. 5a of Ref. 8). The set of parameters yield a Young's modulus $E = 2.561 \text{ eV/\AA}^2$, and a Poisson ratio $\nu = 0.238$, identical to what we obtain in DFT calculation. The computed morphology compares closely to the exact solution to the Föppl-Hencky equation, as shown in Fig. S4.

F. Least-square atomic strain

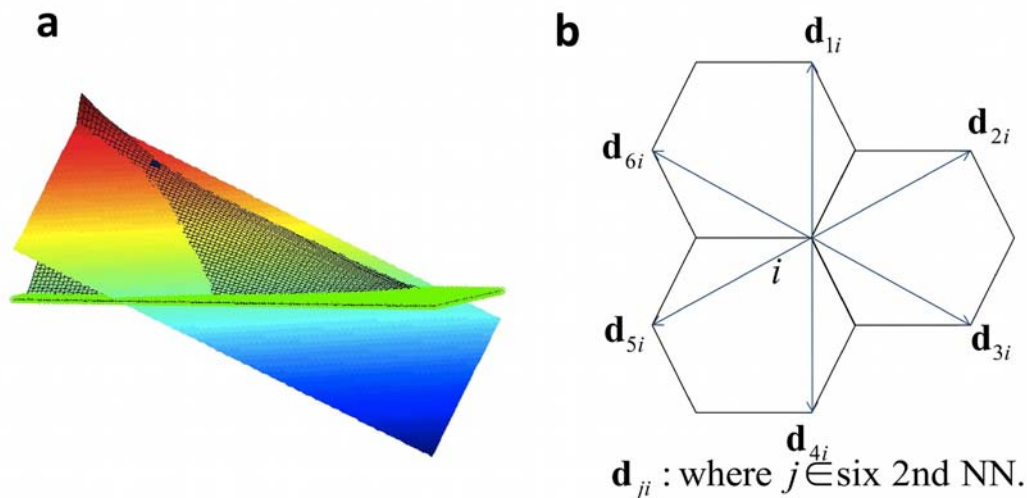


Figure S5 | (a) The tangent plane. (b) Six nearest neighbors included in the calculation of the least-square strain.

The local strain is computed as follows. We compute the surface normal of, say, the i -th atom with a bicubic interpolation of the surface, with which the tangent plane can be located. We then project the initial atomic configuration onto the tangent plane⁹. As shown in Fig. S5a, the curved surface of the deformed membrane is denoted S , and the tangent plane S_i . Six second-nearest neighbors, as shown in Fig. S5b, are selected to compute the least-square atomic strain.^{10,11}

The least-square atomic strain is computed as follows. Let $\mathbf{d}_{ji} = \mathbf{r}_j - \mathbf{r}_i$ for the current configuration, and $\mathbf{d}_{ji}^0 = \mathbf{r}_j^0 - \mathbf{r}_i^0$ for the reference configuration. Then matrices \mathbf{W}_i , \mathbf{V}_i and \mathbf{J}_i are define as,

$$\mathbf{W}_i = \sum_{j=1}^6 \mathbf{d}_{ji}^{0T} \mathbf{d}_{ji}$$

$$\mathbf{V}_i = \sum_{j=1}^6 \mathbf{d}_{ji}^{0T} \mathbf{d}_{ji}^0 \tag{S5}$$

$$\mathbf{J}_i = \mathbf{V}_i^{-1} \mathbf{W}_i$$

With which the strain tensor is:

$$\boldsymbol{\eta}_i = \frac{1}{2} (\mathbf{J}_i \mathbf{J}_i^T - \mathbf{I}) \tag{S6}$$

And the hydrostatic strain invariant is defined as

$$\boldsymbol{\eta}_{\text{hydro,2D}} = \frac{1}{2} \text{Tr } \boldsymbol{\eta}_i \tag{S7}$$

G. Layered patterning of strain-engineered artificial atom arrays

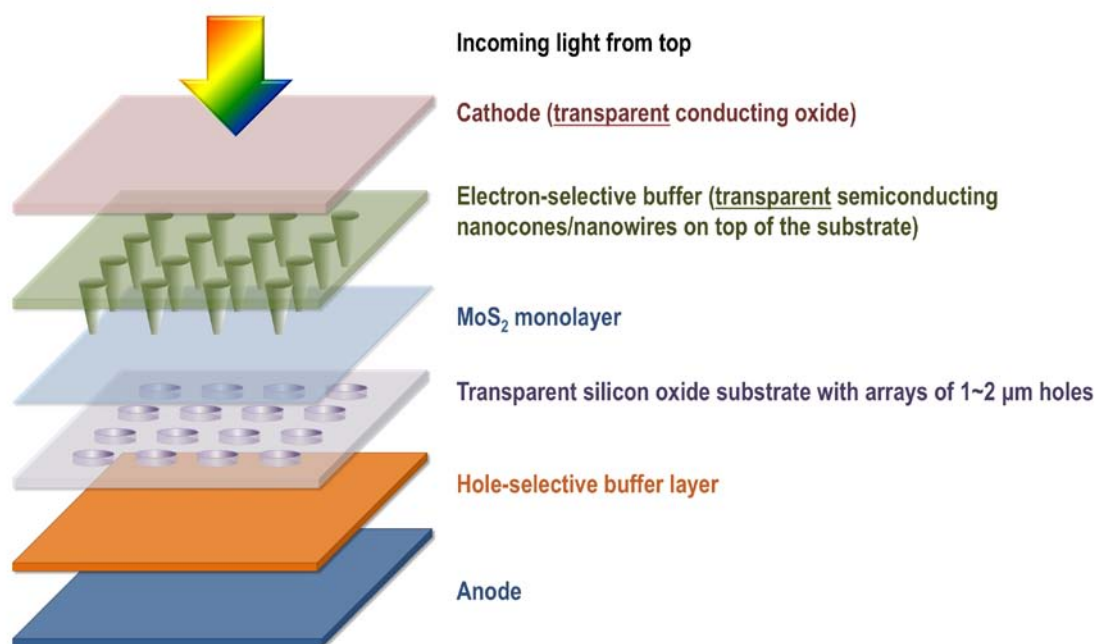


Figure S6 | Layered patterning for achieving arrays of inhomogeneous strain engineered artificial atoms.

References

- Hoffmann, R., Howell, J. M. & Rossi, A. R. Bicapped tetrahedral, trigonal prismatic, and octahedral alternatives in main and transition group six-coordination. *J. Am. Chem. Soc.* **98**, 2484-2492 (1976).
- Cao, T. *et al.* Valley-selective circular dichroism of monolayer molybdenum disulphide. *Nature Commun.* **3** (2012).
- Hohenberg, P. & Kohn, W. Inhomogeneous electron gas. *Phys. Rev. B* **136**, B864-B871 (1964).
- Kohn, W. & Sham, L. J. Self-consistent equations including exchange and correlation effects. *Phys. Rev.* **140**, A1133-A1138 (1965).
- Landau, L. D., Lifshits, E. M., Kosevich, A. M. & Pitaevskii, L. P. *Theory of elasticity*. 3rd English edn, (Pergamon Press, 1986).
- Jin, C. R. Large deflection of circular membrane under concentrated force. *Appl. Math. Mech.-Engl.* **29**, 889-896 (2008).
- Nisoli, C., Lammert, P. E., Mockensturm, E. & Crespi, V. H. Carbon nanostructures as an electromechanical bicontinuum. *Phys. Rev. Lett.* **99**, 045501 (2007).

- 8 Tersoff, J. New empirical-approach for the structure and energy of covalent systems. *Phys. Rev. B* **37**, 6991-7000 (1988).
- 9 Arroyo, M. & Belytschko, T. An atomistic-based finite deformation membrane for single layer crystalline films. *J. Mech. Phys. Solids* **50**, 1941-1977 (2002).
- 10 Shimizu, F., Ogata, S. & Li, J. Theory of shear banding in metallic glasses and molecular dynamics calculations. *Mater. Trans.* **48**, 2923-2927 (2007).
- 11 Falk, M. L. & Langer, J. S. Dynamics of viscoplastic deformation in amorphous solids. *Phys. Rev. E* **57**, 7192-7205 (1998).

LASER FABRICATION

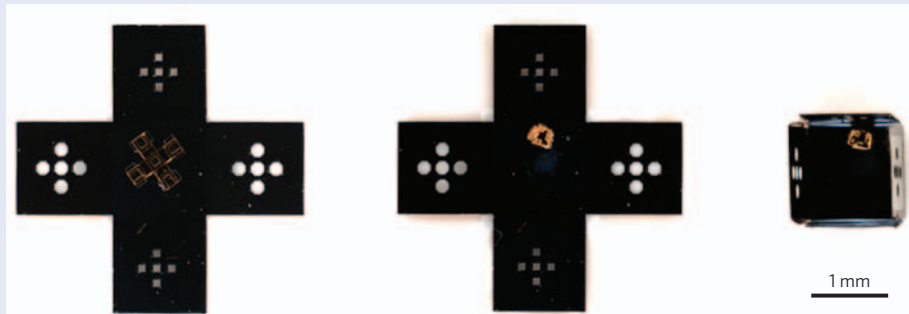
Folding three-dimensional microstructures

The ability to fold microstructures allows the fabrication of complex three-dimensional shapes. Unfortunately, current laser-based folding techniques require the use of extremely intense laser beams reaching thousands of watts per square centimetre.

Now, by exploiting a polymer trigger layer on a pre-stressed metallic bilayer, Kate Laflin and co-workers from John Hopkins University and the US Army Research Laboratory in the USA have developed a laser-triggered sequential folding method that requires a beam intensity of just 680 mW cm^{-2} (*Appl. Phys. Lett.* **101**, 131901; 2012). Their laser-triggered actuation also provides spatial control over the individual hinges, thus allowing three-dimensional patterned cubes to be folded sequentially.

The key to their technique is the hinged actuation, which is based on the intrinsic stress built into metallic thin films. The thin-film hinges contain a layer of chromium, which has high intrinsic stress, and a layer of gold, which has low intrinsic stress. The researchers fabricated their bilayer hinges on copper-coated silicon wafers by vapour deposition and photolithography, and then placed a polymer trigger on top. Bending occurred when the polymer was softened upon heating by laser irradiation.

The team used a commercially available green laser (wavelength of



532 nm, beam power of 40 mW and beam diameter of 1.5 mm) to trigger folding of the smaller cruciform. They then used the same laser to trigger folding of the larger cruciform. This high-precision demonstration of sequential folding across two size scales offers considerable control over the complexity of structures that can be fabricated using laser-triggered actuation.

The researchers also investigated the folding behaviour of various sizes of microstructure, ranging from $300 \mu\text{m}$ to 3 mm, using both the green laser and a near-infrared laser (wavelength of 808 nm, beam power of 100 mW and beam diameter of 3 mm). When the photoresist in each microstructure was heated above $40 \text{ }^\circ\text{C}$, it softened and no longer retained the

stressed bilayer, resulting in spontaneous bending. The time taken for each hinge to close varied between 67 ms and 21 s, depending on the wavelength and intensity of the laser irradiation. By analytically and numerically modelling heat losses from the microstructure, the researchers discovered that the time taken for the hinge to close is determined by thermal conduction into the surrounding air domain, and is therefore proportional to the inverse of the irradiance.

These microdevices could be useful for defence applications such as the remote initiation of energetic materials and for attaching transponder tags or other electronics to various surfaces.

NORIAKI HORIUCHI

OPTICAL MATERIALS

Inspired by strain

Researchers at Peking University and the Massachusetts Institute of Technology propose the use of strain engineering to create a broadband solar 'funnel' in an atomically thin sheet of MoS_2 .

Arend van der Zande and James Hone

Strain engineering is the process of tuning a material's electronic properties by altering its structural or mechanical properties. This technique is widely used throughout the semiconductor industry as a means of enhancing the mobility of electrons in silicon by depositing strained silicon nitride layers on top of transistor channels. The understanding and optimization of strain-engineered materials is also a major

milestone in the international technology roadmap for semiconductors¹. However, the low maximum strains of brittle bulk crystalline materials limit the extent to which their electronic properties can be changed by mechanical means. Bulk silicon, for example, can be strained only 1.2% before breaking, although silicon nanowires with breaking strains of nearly 5% have recently been reported.

The past few years have seen an explosion of interest in two-dimensional (2D) crystals derived from layered materials that possess strong in-plane bonding and weak van der Waals bonding between crystal planes. The most prominent member of this family is graphene; other 2D crystals include hexagonal boron nitride and a number of transition metal dichalcogenides

such as MoS₂, WS₂ and NbSe₂. These materials offer a wide variety of interesting optical and electronic properties. For example, graphene is a highly conductive semimetal, hexagonal boron nitride is a 5.5 eV wide-bandgap semiconductor, and monolayer MoS₂ is a 1.8 eV direct-gap semiconductor². These materials can be fabricated as atomically thin membranes, transferred on to arbitrary substrates and then stacked on top of one another, and can be poked, strained or rippled without breaking. They are also easy to synthesize. Graphene can already be produced in metre lengths using chemical vapour deposition, and rapid progress has been made over the past year in the synthesis of high-quality hexagonal boron nitride, MoS₂ (ref. 3) and WS₂ monolayers.

The 2D sheet geometry of these crystals offers a unique opportunity for studying and utilizing much larger strains than those achievable in bulk (3D) materials. In three dimensions, the ultimate strain is limited by both bulk defects and surface imperfections. 2D crystals can circumvent these limitations for two reasons: first, 2D crystals lack dangling bonds or other imperfections at their surfaces; and second, it is possible to apply highly anisotropic strain to 2D sheets, which limits the strain to a small area inside a single crystalline domain and far from clamping points and edges. These advantages are seen most clearly in graphene, the best-studied 2D material. In experiments, graphene has been seen to withstand elastic strains of up to 25%⁴, which represents the ultimate maximum strain of a perfect carbon lattice. Owing to the large changes in electronic band structure that result under such strain, there is currently great interest in exploiting strain engineering for electronic applications⁵. Moreover, the ability to grow graphene over large areas, combined with its mechanical robustness, has led to a surge of interest in using graphene for flexible electronics. Recent work has demonstrated that other 2D materials share many of the outstanding mechanical properties of graphene: for instance, MoS₂ has a breaking strain of at least 10%⁶. It is likely that the entire family of 2D materials will become a fertile area for exploring and utilizing strain engineering.

Now, writing in *Nature Photonics*, Feng *et al.* consider a new application area of strain engineering in optoelectronic devices⁷. Specifically, they propose a creative new idea in which non-uniform strain applied to an MoS₂ monolayer produces a solar ‘funnel’ that can capture photons with a wide range of energies, thus channelling the resulting electron–hole pairs to a single point for collection. This implementation requires only

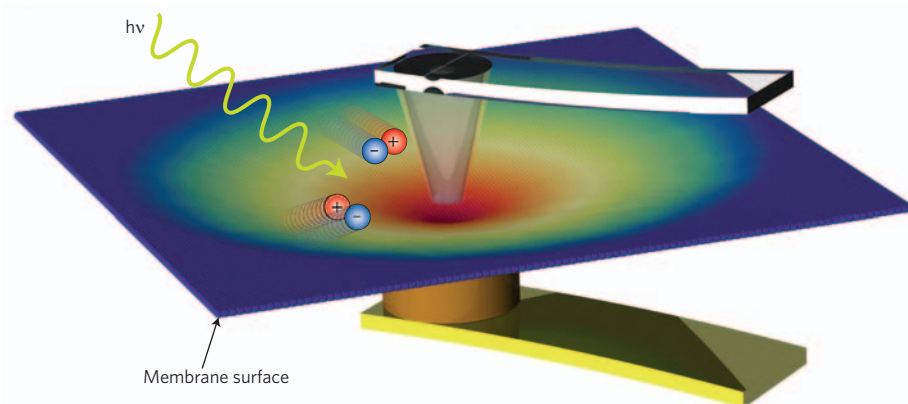


Figure 1 | Solar funnel based on a strained monolayer of MoS₂. Non-uniform strain is induced using an atomic force microscope probe at the centre of the membrane. Light hitting the membrane creates photogenerated electron–hole pairs that drift towards the region of most strain (shown in red) where they are separated and travel to two electrodes, thus generating electricity.

a single sheet of material, whereas previous demonstrations have relied on stacks of graded materials⁸.

By developing theoretical models, Feng *et al.* first show that in-plane tension can be used to tune the bandgap of monolayer MoS₂ continuously from the unstrained value of 1.8 eV all the way down to zero, near a strain of 10%. This result alone, which has also been demonstrated by several other groups⁹, is of significant interest: finding a suitable technique for fixing the strain in the monolayer could allow the bandgap to be set at any arbitrary value. The researchers then propose a new and creative idea of creating spatially varying strain across a single 2D membrane. One of the most unique aspects of a 2D material is the ease at which it can undergo the application of non-uniform strain. In the simplest example, when a suspended circular 2D membrane is indented at its centre, the strain varies almost inversely with radial distance from the centre. For MoS₂ in this geometry, Feng *et al.* show that the bandgap should decrease from the edge to the centre in response to the applied force.

The spatially varying bandgap has two important consequences for the collection of solar energy. First, the bandgap can absorb photons with energies from zero up to the unstrained bandgap of 1.8 eV, which makes the MoS₂ membrane a very wideband absorber. Second, photogenerated excitons (weakly bound electron–hole pairs) created at any point in the membrane will ‘fall’ towards the point of highest strain in the centre of the device, thereby creating a solar energy funnel. In the example studied by Feng *et al.*, these photogenerated electrons and holes are guided to the centre of the membrane

towards an atomic force microscopy tip, which is used as an actuator to apply strain.

The fundamental challenge when making a practical solar funnel is how to separate the electron–hole pairs and transport the charge to electrodes so that electricity can be successfully extracted. In conventional photovoltaics, a built-in electric field at a p–n junction separates the electrons and holes. The positive and negative charges are then collected at different locations by placing electrodes on opposite sides of the exciton-generating material. However, in the MoS₂ solar funnel, both the electrons and holes are funnelled to a single point. To resolve this issue, Feng *et al.* say that two electrodes composed of metals with different work functions placed at the centre point could be used to selectively remove the electrons and holes. Although this approach might work, it introduces several experimental and material challenges. For example, monolayer MoS₂ does not provide a sufficiently large barrier to quantum tunnelling between different electrodes. As a result, parasitic tunnelling will probably prevent generation of a significant open-circuit voltage, which is a key performance metric for an efficient solar cell. One solution to this problem could be to use an applied electric field to break the electron–hole symmetry, thereby allowing the electrons to be collected in the centre of the membrane, while holes could be collected at the edge. Another approach might be to place the MoS₂ on a nanostructured surface (such as a periodic array of steps or holes) rather than suspending it over large holes. The van der Waals adhesion to the substrate would pull down the membrane and induce

spatially varying tension; by carefully placing the electrodes over strained and unstrained regions, the electrons and holes could then be collected separately.

At a fundamental level, the work of Feng *et al.* demonstrates that the strain engineering of 2D materials has many potential applications beyond electronics, and it is likely that these findings will inspire many more investigations into this rich field. For example, it would be interesting to study stacked

heterostructures of these materials. For solar collection, such a heterostructure could allow the vertical separation of electrons and holes, while strain could then be used to guide diffusion to opposite electrodes.

Arend van der Zande and James Hone are at the Department of Mechanical Engineering and Energy Frontier Research Center, Columbia University, 500 West 120th Street, New York, USA. e-mail: jh2228@columbia.edu

References

1. <http://www.itsrs.net/home.html>
2. Mak, K. F., Lee, C., Hone, J., Shan, J. & Heinz, T. F. *Phys. Rev. Lett.* **105**, 136805 (2010).
3. Lee, Y.-H. *et al. Adv. Mater.* **24**, 2320–2325 (2012).
4. Lee, C., Wei, X. D., Kysar, J. W. & Hone, J. *Science* **321**, 385–388 (2008).
5. Pereira, V. M. & Castro Neto, A. H. *Phys. Rev. Lett.* **103**, 046801 (2009).
6. Bertolazzi, S., Brivio, J. & Kis, A. *ACS Nano* **5**, 9703–9709 (2011).
7. Feng, J., Qian, X., Huang, C.-W. & Li, J. *Nature Photon.* **6**, 866–872 (2012).
8. Kramer, I. J., Levina, L., Debnath, R., Zhitomirsky, D. & Sargent, E. H. *Nano Lett.* **11**, 3701–3706 (2011).
9. Yun, W. S., Han, S. W., Hong, S. C., Kim, I. G. & Lee, J. D. *Phys. Rev. B* **85**, 033305 (2012).

VIEW FROM... 73RD JSAP AUTUMN MEETING 2012

The search for high efficiency

Tandem solar cells, inverted triple-junction solar cells and photonic-crystal-based solar cells were among the photovoltaic devices discussed at the 73rd Autumn Meeting of the Japan Society of Applied Physics.

Noriaki Horiuchi

The Fukushima nuclear disaster of 2011 has placed increasing pressure on the search for alternative energy sources in Japan, and high-conversion-efficiency solar cells are in high demand. It is unsurprising, therefore, that photovoltaic technology was the highlight of this year's Japan Society of Applied Physics (JSAP) Autumn Meeting, held on 11–14 September in Matsuyama. The meeting gathered 5,700 researchers at the campuses of Ehime and Matsuyama Universities.

In April 2012, the Ministry of Education, Culture, Sports, Science and Technology of Japan assigned Makoto Konagai from the Tokyo Institute of Technology as the Director of Renewable Energy Projects to coordinate research projects ranging from fundamental studies to the commercialization of silicon-based tandem solar cells. These projects are being carried out jointly by academia and industrial collaborators such as Panasonic, Mitsubishi and Kaneka. At the meeting, Konagai, who is also the president of JSAP, announced the launch of Centres of Excellence for solar cells based on silicon nanowires in April 2014 in the Fukushima prefecture. Research performed at these centres will focus on tandem solar cells comprising silicon nanowires on the top layer and conventional silicon solar cells on the bottom layer.

"It is difficult to achieve conversion efficiencies of more than 25% by using conventional silicon-based solar cells because silicon cannot absorb the spectrum of natural sunlight from 1.4 to 1.7 eV, where a fair amount of the energy is distributed," Konagai pointed out. Devices based on silicon



NORIAKI HORIUCHI

Around 5,700 participants attended the Autumn Meeting of JSAP 2012, which was co-hosted by Ehime and Matsuyama Universities.

nanowires are a different matter altogether. At the meeting, Konagai's research group presented numerical results for tandem solar cells reaching conversion efficiencies of more than 30%.

Atsushi Yoshida from Sharp reported an inverted InGaP/GaAs/InGaAs triple-junction cell with a conversion efficiency of 43.5%. "This conversion efficiency is due to the reduction of current loss by using InGaAs, which has a bandgap of 1 eV, as the bottom cell," Yoshida explained. However, this approach is far from straightforward because the large difference in lattice

constants between InGaAs and InGaP (or GaAs) degrades the crystalline quality and thus increases the current loss. To overcome this problem, Yoshida's group developed an inverted deposition method for growing the disconformable bottom cells at the end of deposition procedure and a technique for printing the InGaP/GaAs/InGaAs triple-junction cells on a supporting substrate. As a result, they succeeded in obtaining a record-breaking solar-cell conversion efficiency of 43.5% under 306-Sun conditions.

The ability to convert broadband thermal emission into a narrowband spectrum with